Reaction kinetics of protons and oxide ions in LSM/ lanthanum tungstate cathodes with Pt nanoparticle activation

Ragnar Strandbakke[1]*, Oddvar Dyrlie[1], Fredrik Sydow Hage[2,3]**, Truls Norby[1]

[1]Centre for Materials Science and Nanotechnology, Department of Chemistry, University of Oslo, FERMiO, Gaustadalleen 21, NO-0349 Oslo, Norway

[2] Institute for Energy Technology, Physics Department, NO-2007 Kjeller, Norway

[3] Department of Physics, University of Oslo, NO-0316 Oslo, Norway

[*] Corresponding author: Ragnar Strandbakke. e-mail: ragnarst@smn.uio.no ,

Phone: +47-22 84 06 60

[**] Now at: SuperSTEM Laboratory, SciTech Daresbury, Keckwick Lane, Daresbury, WA4 4AD, UK

Abstract

Composite electrodes of $La_{0.8}Sr_{0.2}MnO_3$ (LSM) / $La_{28-x}W_{4+x}O_{54+3x/2}$ (x=0.85, "LWO56") on LWO56 electrolytes have been characterized by use of electrochemical impedance spectroscopy vs pO_2 and temperature from 900 °C, where LWO56 is mainly oxide ion conducting, to 450 °C, where it is proton conducting in wet atmospheres. The impedance data are analyzed in a model which takes into account the simultaneous flow of oxide ions and protons across electrolyte and electrodes, allowing extraction of activation energies and pre-exponential factors for the partial electrode reactions of protons and oxide ions. One composite electrode was infiltrated with Pt nanoparticles with average diameter of 5 nm, lowering the overall electrode polarization resistance (R_p) at 650 °C from 260 to 40 Ω cm^2. The Pt-infiltrated electrode appears to be rate limited by surface reactions with activation energy of ~90 kJ mol^{-1} in the low temperature proton

transport regime and ~150 kJ mol^{-1} in the high temperature oxide ion transport regime. The charge transfer reaction, which makes a minor contribution to R_p, exhibits activation energies of ~85 kJ mol^{-1} for both oxide ion and proton charge transfer.

1. Introduction

Solid oxide fuel cells (SOFCs) with proton conducting electrolytes (also called proton ceramic fuel cells, PCFCs) have the potential benefit that they, due to higher bulk mobilities of protons vs oxide ion defects, can operate with higher efficiency at lower temperatures than oxide ion conducting SOFCs. Moreover, water formation on the oxygen side instead of the fuel side prevents diluting the fuel, and hence, PCFCs can operate with higher fuel efficiency, simpler balance-of-plant, and reduced risk of anode oxidation. One of the main obstacles so far for utilizing the full potential of PCFCs is the poor performance of the cathode, and state-of-the-art SOFC cathode materials based on oxide mixed ion electron conducting electrode materials (O-MIECs) has not yet shown acceptable performance for PCFCs at intermediate temperatures [1]. In a fuel cell with protons as the only charge carriers, all faradaic current is in principle restricted to pass through the triple phase boundary (tpb) when supplied with O-MIEC or pure electron conducting electrodes. Since the surface kinetics for the reactions preceding water formation in the tpb region is normally slow at low temperatures, they will potentially limit the overall rate of the PCFC cathode reaction. As there are still only a few mixed proton electron conducting (P-MIEC) oxides reported as PCFC cathode materials [2-4], a PCFC is therefore more vulnerable to slow kinetics and diffusion at the electrode surfaces than the oxide ion conducting SOFC. Figure 1 illustrates the reaction paths for an O-MIEC electrode on an oxide-ion conductor (a) and on a proton conductor (b), a P-MIEC electrode on a proton conductor (c), and a pure electronic conductor electrode on oxide ion (d) and proton conducting (e) electrolytes. As can be seen for the proton conducting systems in Figure 1 b) and e), oxygen kinetics at the surfaces around tpb is critical, even if the electrode material is an O-MIEC. A way of enhancing this surface kinetics may be to add nano-sized oxygen catalysts such as Pt to the porous electrode structure. The nano catalysts will also facilitate an increase in active triple phase reaction sites.

Strontium doped lanthanum manganite, $La_{1-x}Sr_xMnO_3$ (LSM), is one of the most studied cathode materials for high temperature SOFCs [5-9]. Due to its moderate O-MIEC properties at high temperatures, LSM is considered to exhibit acceptable performance for SOFCs at temperatures of 900 °C and above. At lower temperatures, LSM is more or less a pure electronic (hole) conductor, and shows high cathodic overpotential both for proton conducting [10, 11] and oxide ion conducting systems [12]. In this work we study the LSM composition $La_{0.8}Sr_{0.2}MnO_3$ as cathode material on the ionic conductor lanthanum tungstate, $La_{28-x}W_{4+x}O_{54+3x/2}$ (x=0.85, with ratio La/W ≈ 5.60; "LWO56"). LWO56 is mainly proton conducting in wet atmospheres at low temperatures, while oxide ion conduction takes over with increasing temperature. This makes LWO56 suitable as electrolyte material in a study of the rate limiting cathode processes over the whole temperature range, from protonic transport at low temperatures, to oxide ionic transport at higher temperatures.

In order to provide sufficient tpb reaction sites, a 50 / 50 vol% LSM / LWO56 composite electrode is used in this study. To further meet the challenge of slow oxygen kinetics at low temperatures, we infiltrate one composite LSM / LWO56 cathode with a suspension of Pt nanoparticles with diameters of ~5 nm before performing electrochemical impedance spectroscopy (EIS) in the temperature range 450-900 °C. Moreover, dependencies of partial polarization resistances on pO_2 were investigated at 700, 800 and 900 °C on a Pt-free composite electrode.

The characterization of the partial electrode resistances involves a novel way of modelling the deconvoluted EIS data, seeing the flow of protons and oxide ions as parallel charge carrier paths or "rails" [4]. By doing this, activation energies and pre-exponential values for components adding up to the total polarization resistance can be obtained. Activation energies are useful "labels" for elementary reaction steps, and possible shifts in apparent activation energies and pre-exponential values will give indications on shifts in dominating rails and rate limiting reaction steps. Kinetic parameters for reactions at the surface and electrode / electrolyte interface often entail charge transfer resistance, $R_{p,ct}$, to be a more dominant part of the total R_p at high temperature, while diffusion and/or surface related polarization resistance, $R_{p,d}$, often limits the reaction rate at lower temperatures. In addition, charge carrier characteristics of electrode and electrolyte materials may change over the measured temperature range, altering the reactions that make up $R_{p,ct}$ and $R_{p,d}$. In this work, we study the effect on $R_{p,ct}$ and $R_{p,d}$ as the electrolyte material changes

from being a high temperature oxide ion conductor, through a transition temperature region of mixed ionic conductivity, to exhibiting pure proton conductivity at lower temperatures.

2. Theory

The ionic transport through an electrolyte like LWO56 takes place by a mixture of protons and oxide ion defects, depending on temperature and $p\mathrm{H_2O}$. Each type of charge carrier undergoes red-ox at the oxygen electrode, and elementary reaction steps should be described accordingly. Figure 2 is a schematic electric circuit of such a mixed conducting system, with partial resistances in each charge carrier rail. In EIS, we typically obtain two distinguishable partial R_p's: One at high frequencies assigned to charge transfer across the electrolyte / electrode interface ($R_{p,ct}$), and one at lower frequencies, comprising surface exchange and diffusion related processes on the surface or inside the electrode material ($R_{p,d}$), hereafter denoted diffusion for brevity. The electrical charge transfer, e.g., the ionization of surface species is not easily distinguishable from the interface charge transfer reaction and will fall into the high frequency arc. Both $R_{p,ct}$ and $R_{p,d}$ have parallel contributions from protons and oxide ions, and they are connected in series to the respective area-specific resistances R_{v,H^+} and $R_{v,O^{2-}}$ arising from the partial ionic volume conductivities of the electrolyte. The resistances deconvoluted from EIS, R_v, $R_{p,ct}$ and $R_{p,d}$ can thus be represented by a model of two parallel charge carrier rails, comprising the series connection of R_{v,H^+}, R_{p,ct,H^+} and R_{p,d,H^+} in the proton transport rail, and $R_{v,O^{2-}}$, $R_{p,ct,O^{2-}}$ and $R_{p,d,O^{2-}}$ in the oxide ion transport rail. These partial resistances for protons and oxide ions can, in turn, be represented by transport and rate equations, where the parameters are fitted to T and $p\mathrm{O_2}$.

The parallel transport of protons and oxide ion defects may give rise to interactions between the two charge carriers in the bulk of the materials, constituting an internal chemical storage of water by hydration and dehydration, with capacitive behavior [13, 14]. We do not see indications that this plays a major role in the present system, but we cannot exclude it. However, in the absence of simple analytical ways of integrating such chemical capacitances in the model, and in order not to add to the complexity of the model, we will disregard them onwards here.

Figure 3 gives a typical Nyquist plot, taken of the Pt-infiltrated LSM / LWO56 composite electrode at 600 °C in wet oxygen. When deconvoluting it, the intercept with the real axis, marked as S0 in Figure 3, represents the area-specific electrolyte volume resistance, R_v, given as

$$R_{S0} = R_v = \frac{1}{\frac{1}{R_{v,H^+}} + \frac{1}{R_{v,O^{2-}}}} \tag{1}$$

The next point, shown as S1 in Figure 3, represents the serial sum of R_v and the first part of the area-specific polarization resistance, namely the charge transfer resistance, $R_{p,ct}$. More precisely, the resistance in S1, R_{S1}, is a parallel connection of the oxide ion and proton rails where each has volume and charge transfer contributions. We may thus write

$$R_{S1} = R_v + R_{p,ct} = \frac{1}{\frac{1}{R_{v,H^+} + R_{p,ct,H^+}} + \frac{1}{R_{v,O^{2-}} + R_{p,ct,O^{2-}}}} \tag{2}$$

In the same manner S2, apparently representing the serial connection of R_v, $R_{p,ct}$ and $R_{p,d}$, is also a parallel connection of the oxide ion and proton rails, each now with volume, charge transfer and diffusion contributions:

$$R_{S2} = R_v + R_{p,ct} + R_{p,d} = \frac{1}{\frac{1}{R_{v,H^+} + R_{p,ct,H^+} + R_{p,d,H^+}} + \frac{1}{R_{v,O^{2-}} + R_{p,ct,O^{2-}} + R_{p,d,O^{2-}}}} \tag{3}$$

If it should be expedient to represent the data by apparent partial resistances $R_{p,ct}$ and $R_{p,d}$, the first is found by $R_{S1} - R_{S0}$ and the latter by $R_{S2} - R_{S1}$. When fitting experimental ASRs at S0 to find R_{v,H^+} and $R_{v,O^{2-}}$, one may use independent information such as partial electrolyte conduc-

tivities, hydration thermodynamics, or parameters for proton and oxygen vacancy mobilities from literature.

The partial resistances for electrolyte volume, charge transfer and diffusion can be expressed for protons and oxide ions by conductivities and electrode reaction expressions in terms of enthalpies, pre-exponentials and pressure dependencies. First, we obtain volume conductivities for protons and oxide ions. By assuming that bulk transport is dominating the transport in the electrolyte, the partial volume conductivities are given by

$$\sigma_{v,H^+} = Fz_{H^+}\mu_{H^+}c_{H^+} = F\left[OH_O^{\bullet}\right]d_m\frac{1}{T}\mu_{H^+}^0\exp\left(\frac{-\Delta H_{mob,H^+}}{RT}\right) \quad (4)$$

$$\sigma_{v,v_O^{\bullet\bullet}} = Fz_{v_O^{\bullet\bullet}}\mu_{v_O^{\bullet\bullet}}c_{v_O^{\bullet\bullet}} = F\left(4-3x-\left[OH_O^{\bullet}\right]\right)d_m\frac{1}{T}\mu_{v_O^{\bullet\bullet}}^0\exp\left(\frac{-\Delta H_{mob,v_O^{\bullet\bullet}}}{RT}\right) \quad (5)$$

Here, d_m is molar density, $4 - 3x$ represents the concentration of oxygen vacancies in the dry state [15], given by the *W*-excess, *x*, and μ^0 is the pre-exponential mobility factor for each charge carrier. If we plot $\ln(\sigma_v T)$ vs 1/T in the range 450-900 °C and use pre-defined enthalpies for each charge carrier mobility [16] as well as a general concentration expression for protons [17] containing standard hydration entropy and enthalpy [18], pre-exponential mobility factors for each partial conductivity in the electrolyte can be extracted through equations 4 and 5. Area-specific partial volume resistances are obtained by

$$R_{v,i} = \frac{l}{\sigma_{v,i}} \quad (6)$$

, where *l* is the electrolyte thickness. In this work, a three electrode set up is deployed, and by applying the working and reference electrodes on opposite sides of the button cell, we assume that *l* can be approximated by the full sample thickness.

For charge transfer and diffusion in the case of protons or oxide ions, each partial polarization resistance is written as standard activated rate expressions with dependencies on pO_2 and pH_2O:

$$\frac{1}{R} = FpO_2^n pH_2O^m A^0 \exp\left(\frac{-E_A}{RT}\right) \quad (7)$$

Here, A^0 is the pre-exponential "mobility" factor, containing the area-specific molar attempt rate, and E_A is the activation energy of the elementary electrode reaction step with resistance R for each ionic charge carrier. In order to relate A^0 directly to area-specific resistance, we will in the following present the pre-exponential factor as what may be labelled an "exchange resistance", R^0:

$$R^0 = \frac{1}{FA^0} \quad (8)$$

The fitting of the equations to the measured data is done in three steps. R_v at S0 is the resistance representing the parallel transport of protons and oxide ions in the electrolyte. In the first step, R_v is fitted to Equations (1) and (4-6), separated into partial area-specific resistances. In the second fitting step, parameters for R_{v,H^+} and $R_{v,O^{2-}}$ are kept constant, while the parameters for the proton and oxide ion charge transfer polarizations are fitted to experimental values of R_{S1} using Equations (2) and (7). In the third step, measured values of R_{S2} are fitted to Equation (3) and (7), yielding parameters for R_{p,d,H^+} and $R_{p,d,O^{2-}}$. The parameters for R_{p,ct,H^+}, $R_{p,ct,O^{2-}}$ and partial volume resistances obtained in the two first steps of fitting are fixed and used in fitting values of R_{S2} to Equation (3).

3. Experimental

3.1 Sample preparation

Powder of LWO56 ($La_{27.15}W_{4.85}O_{55.28}$, CerPoTech, Norway) was uniaxially pressed into disks, 20 mm in diameter at 140 MPa, and sintered at 1500 °C for 4 hrs. $La_{0.8}Sr_{0.2}MnO_3$ (LSM) was made by spray pyrolysis from nitrate salts. The resulting LSM powder was ball milled and sieved (250 nm). Ink of a mixture of LSM (50 vol%) and LWO56 (50 vol%) was prepared by ball milling the proper ratio of powders in isopropanol for 1 hr at 250 rpm. 3.4 g of powder mixture was

ground in a mortar with 0.5 mL of Solsperse 8000 dispersing agent (Lubrizol, UK) to a thick paste. This was washed in 10 mL of isopropanol and mixed with 10 mL of terpineol. Finally, 15 g of 10 % ethyl cellulose in isopropanol solution was added, and the paste was stir-mixed and evaporated for three days, until the proper viscosity was achieved. The symmetrical cell was made by brush painting electrodes, 10 mm in diameter, in one layer on each side of the LWO56 pellet. The sample was dried for 1 hr at 100 °C and fired at 1200 °C for 4 hrs. The symmetrical cell was used for pO_2-dependency measurements.

Two pellets of LWO56 were prepared for the temperature-dependency measurements. On the bottom side, 10 mm diameter Pt electrodes (Metalor 6926) were brush-painted as counter electrodes, and at the sample bottom circumferences, Pt paste was brush-painted to act as reference electrode. The Pt electrodes were fired at 1100 °C for 1 hr. Circular composite electrodes of LSM / LWO56 were brush-painted on the top side of both pellets and fired at 1200 °C for 4 hrs. One sample was impregnated with Pt nanoparticles (see below), and one was left untreated for comparison.

3.2 Synthesis, application and characterization of Pt nanoparticles

Pt nanoparticles were prepared by methanol reduction of aqueous H_2PtCl_6 (8 wt %, Sigma Aldrich 262587) [19, 20]: 5 mL 50 vol% methanol in water (VWR 20847.295) and 0.0563 g H_2PtCl_6 were mixed. 200 µL 0.1 M sodium citrate (Sigma Aldrich W302600) was added as stabilizer. Reflux vas carried out at 80 °C in a test tube with magnetic stir and condenser. After 20 min, the solution turned black, and after 25 minutes the test tube was immersed in cold water to stop the reaction.

The black Pt sol was then added to 10 mL 3 mM oleylamine (Sigma Aldrich 07805) as phase transfer agent to hexane. Shaking by hand for three minutes gave a clear aqueous phase and a black hexane phase. The aqueous phase was separated out, and the remaining hexane Pt sol was evaporated in an open vessel on a hot plate at 60-70 °C, and purified with 5 mL ethanol. In ethanol, Pt nanoparticles agglomerated to a spongy precipitate. It was separated from ethanol in a lab centrifuge and dried in air. Washing removes uncoordinated oleyleamine. The Pt precipitate was redispersed in 2 mL octane under treatment in ultrasonic bath. Characterization of the

particles was done by means of High Resolution Transmission Electron Microscopy (HRTEM) on a Jeol JEM 2010F operated at 200 kV. TEM specimens were prepared by sonication of the powder suspended in ethanol and subsequent dispersion onto a holey carbon TEM grid.

Impregnating the LSM / LWO56 cathode with Pt nanoparticles was done by dripping four times with 10 µL of Pt sol and drying the electrode at 130 °C in a heating cabinet after each drip. The concentration of Pt in the sol was estimated to 1 mg/mL, and the load of Pt on the electrode 0.03 mg/cm^2.

3.3 Electrochemical measurements

The symmetrical sample used for pO_2 dependency measurements was mounted in a ProboStat sample holder (NorECs, Norway), where EIS was carried out at 700, 800 and 900 °C, in the frequency range 100 kHz - 1 mHz and at 30 mV oscillating voltage with a HIOKI 3522-50 LCR Hitester. Impedance measurements were done as a function of pO_2, isothermally at each temperature step.

The temperature dependency measurements were performed with a Novocontrol Alpha A frequency analyzer in a three electrode set up. The Pt-infiltrated sample was measured stepwise every 50 °C from 900 to 450 °C in wet oxygen. The non-infiltrated sample was measured under the same conditions as the Pt-infiltrated sample; also in a three electrode setup, at 850-650 °C. Below 650 °C the low frequency part of the spectrum was too incomplete to allow deconvolution.

Current collection was done by pressing a gold mesh supplied with spring loads onto each side of the symmetrical sample. On the non-symmetric sample, gold mesh was used as current collector, pressed down on the working and counter electrodes, while the reference electrode, painted in a ring around the counter electrode, was contacted with a flat-pressed ring of Pt wire according to Figure 4. Feed gases were O_2 (99.5 %), air and Ar (99.999 %), where a fixed partial pressure of H_2O (0.027 atm) was obtained by passing the gas through a two-step wetting stage at room temperature; the first stage with pure H_2O and the second with a saturated solution of KBr in H_2O.

Deconvolution of EIS data was done by fitting the impedance data to a Randles-type equivalent circuit with constant phase elements (CPE) as capacitive circuit elements. At lower temperatures

and oxygen pressures, the low frequency dispersion exhibited a drop-shape semi-circle closing, and was therefore deconvoluted with a Gerischer element in series with the Randles circuit. The DC resistance associated with the Gerischer element was added to the diffusion part of the resistance in modelling of partial resistances. Figure 5 gives the deconvolution model. The high frequency intercept on the real axis in the Nyquist plot was set as the parallel combination of ionic volume resistance in the LWO56 electrolyte.

4. Results and discussion

4.1 Nano-sized Pt particles

HRTEM micrographs of the Pt nanoparticles dispersed on a holey carbon TEM grid are shown in Figure 6 and Figure 7. As can be seen from the micrograph in Figure 6, the size distribution is relatively uniform, with diameters in the range 2-5 nm, and little agglomeration is seen, enabling effective infiltration into the porous electrode microstructure.

4.2 Electrode microstructure

Post analysis by SEM showed well-adhered electrode layers with thickness of ~10 μm. The electrode layers had sufficient porosity and small grains (d: ~0.5 μm) in a well-connected grid. The elemental analysis, performed by Energy-Dispersive X-Ray Spectroscopy (EDS) showed no sign of secondary phases between LSM and LWO. Figure 8 shows cross sectional micrographs of the electrode layers on the symmetric sample (a) and Pt infiltrated sample (b). EDS showed traces of Pt (~1.5 atomic %), but no particles could be imaged. The Pt particles are most probably too small to be properly imaged / measured by SEM, even after coarsening at high temperatures.

4.3 Temperature dependencies

In Figure 9, we show a Nyquist plot with fitted model results for the Pt-infiltrated sample at 500 °C in wet oxygen according to the deconvolution model presented in Figure 5. As can be seen from the example at 500 °C, the deconvolution exhibits good agreement with measured data. The deconvoluted R_p's for Pt-infiltrated and non-infiltrated samples in wet O_2 are shown in Figure 10,

along with the modelled partial resistances, $R_{p,ct}$ and $R_{p,d}$ for the Pt-infiltrated sample. The deconvoluted area-specific electrolyte volume resistance, R_v, and deconvoluted $R_{p,ct}$ and $R_{p,d}$ for the Pt-infiltrated sample were fitted to Equations 2 and 3 to model the partial electrode resistances for protons (R_{p,ct,H^+} and R_{p,d,H^+}) and oxide ions ($R_{p,ct,O^{2-}}$ and $R_{p,d,O^{2-}}$). The modelled $R_{p,ct}$ and $R_{p,d}$ are shown as dashed lines in Figure 10. The solid line is the modelled R_p, which is the series sum of modelled $R_{p,ct}$ and $R_{p,d}$. The total polarisation resistance R_p for the Pt-infiltrated electrode is dominated by $R_{p,d}$ at all temperatures except at 900 °C where charge transfer limits the electrode reaction. The total R_p for the non-infiltrated sample ranged from 18 Ωcm^2 at 850 °C to 260 Ωcm^2 at 650 °C. The Pt-infiltrated sample was measured in the range 900-450 °C exhibiting clearly lower R_p over the whole temperature range; 3 and 40 Ωcm^2 at 850 and 650 °C, respectively. There is a slight bend in Arrhenius-type plot at 600-750 °C, coinciding with the temperature region where LWO56 changes from being mainly proton to mainly oxide ion conducting.

The high capacitance and hence low frequency group of processes, which may involve gas diffusion, surface exchange, red-ox of oxygen species and surface diffusion, here characterised in terms of diffusion resistances and labelled $R_{p,d}$, will probably involve oxygen or oxide species. In Figure 10, a gradual change in apparent activation energy is seen for $R_{p,d}$ from high to low temperature. This indicates that the surface oxygen reaction in some way may be related to the nature of the electrolyte charge carrier (oxide ions vs protons).

The fitting yielded R^0, containing inverse area-specific molar attempt rates, and activation energies for the partial charge transfer and high capacitance electrode resistances for protons (R_{p,ct,H^+} and R_{p,d,H^+}) and oxide ions ($R_{p,ct,O^{2-}}$ and $R_{p,d,O^{2-}}$) as shown in Table 1. What can be seen is that the attempt rates and activation energies are similar for protons and oxide ions in the charge transfer reaction. The two surface processes, R_{p,d,H^+} and $R_{p,d,O^{2-}}$ differ, with low attempt rate and activation energy for the former and high attempt rate and activation energy for the latter. These parameters indicate a larger surface reaction area for the species connected to the oxide

ion rail than for the ones connected to the proton rail. The surface reaction in the protonic rail is on the other hand less energy demanding.

In Figure 11, we again plot the deconvoluted values of R_p for the Pt-infiltrated sample. The dashed lines now represent modelled polarization resistances for protons (R_{p,H^+}) and oxide ions ($R_{p,O^{2-}}$) while the solid line is the modelled parallel combination of the two ionic R_p's. In agreement with the ionic transport in LWO56, oxide ions dominate the transport and hence polarization resistance at high temperatures and protons at low. To further visualize the partial resistances of protons and oxide ions, we present the modelled total and partial polarization resistances for protons (R_{p,H^+}, R_{p,ct,H^+} and R_{p,d,H^+}) and oxide ions ($R_{p,O^{2-}}$, $R_{p,ct,O^{2-}}$ and $R_{p,d,O^{2-}}$) vs inverse temperature in Figure 12 and Figure 13, respectively. As before, the solid line represents the modelled parallel combination of R_{p,H^+} and $R_{p,O^{2-}}$. The charge transfer reaction is a minor contribution in both ionic rails at intermediate to low temperatures. At high temperature, the higher attempt rate for the surface reaction gives faster surface kinetics and thus a lowered $R_{p,d,O^{2-}}$ in the dominant oxide ion rail. The comparably lower attempt rate and lower activation energy for $R_{p,ct,O^{2-}}$ makes the charge transfer reaction dominant at high temperature. It is reasonable to suggest that the surface reaction limiting the proton rail is confined to the area close to the triple phase boundary, given the attempt rate similar to the proton charge transfer step. The surface reaction in the oxide ion rail, however, seems spread to a wider surface area, given the higher attempt rate for $R_{p,d,O^{2-}}$. Considering both the attempt rates and the activation energies for the surface reaction, we suggest that the protons undergo a surface process in the vicinity of the triple phase boundary, while the oxide ions undergo a surface reaction with higher energy barrier, but with a wider active reaction zone at the highest temperatures.

Regarding the charge transfer reaction, the results indicate that both oxide ions and protons are confined to pass through the tpb, exhibiting similar attempt rates and activation energies for the two species. The ionic conductivity in LSM at 900 °C is reported to be as low as $5 \cdot 10^{-6}$ Scm^{-1} [21] and $8 \cdot 10^{-8}$ Scm^{-1} [22]. This low ionic conductivity also indicates a reaction path for both protons and oxide ions mostly through the tpb, as shown in Figure 1d) and e).

4.3.1 Diffusion resistances

The activation energies of the rate limiting reaction step for mass transport at or in the electrode (here termed diffusion resistance, $R_{p,d}$) for oxide ions and protons, $R_{p,d,O^{2-}}$ and R_{p,d,H^+}, respectively, can be compared to reported values of E_A for the surface process from previous studies of LSM on oxide ion conducting electrolytes [23-25] as well as on LWO electrolytes [10, 11]. The reported values of E_A for the surface process differ in literature, but are in general reported between 160-200 kJ mol^{-1} at high temperatures, both for oxide ion and proton conductors. In our work, the fitting of the SOFC-like surface reaction, $R_{p,d,O^{2-}}$, yields an activation energy of ~150 kJ mol^{-1}, i.e., in the lower range.

The activation energy for R_{p,d,H^+} is only 90 kJ mol^{-1}, considerably lower than the ~150 kJ mol^{-1} for $R_{p,d,O^{2-}}$. One explanation for the lower activation energy for the surface proton reaction might be that the PCFC reaction is prone to utilizing possible surface hydroxyls in the overall electrode reaction. Surface processes, *i.e.*, dissociative adsorption and diffusion of oxygen on the LSM surface is a commonly proposed rate limiting reaction step for LSM in the SOCF oxygen reduction reaction. Hydroxyl surface diffusion on LSM might be faster than the diffusion of oxide ions. The surface reaction will also be influenced by the infiltrated Pt nanoparticles. Under similar conditions, a Pt electrode facilitates formation of hydroxyls from oxygen and water in cathodic operation. The subsequent surface diffusion of OH is rate determining for the Pt electrode and exhibits an activation energy of ~100 kJ mol^{-1}, as we will show in a new study soon to be published [26]. We have not been able to find reports on the catalytic power of LSM for surface water splitting.

The activation energy of diffusion resistance for LSM on a LWO electrolyte in the temperature-range 600-750 °C has been reported to 118 kJ mol^{-1} [10], considerably lower than the activation energy of 184 kJ mol^{-1} reported in the temperature-range from 700 to 900 °C [11]. Again, it seems that the surface diffusion is less energy demanding at lower temperatures where protons to a larger extent dominate the charge transport. The activation energy for the surface proton reaction, R_{p,d,H^+} obtained in this study is even lower than reported for the temperature-range 600-750 °C. If surface hydroxyls and oxide ions are the diffusing species, and hydroxyls are the faster

of the two, it seems reasonable that they are utilized to a larger extent at lower temperatures where protons dominate. At lower temperatures, R_{p,d,H^+} is dominating over $R_{p,d,O^{2-}}$. Since the sample is measured to lower temperatures, passing the transition temperature and entering the pure proton conductor temperature range, the model allows extraction of more reliable values for the parameters of R_{p,d,H^+}. The previously reported intermediate temperature value of 118 kJ mol^{-1} for the activation energy of $R_{p,d}$ is in good agreement with our model if we consider the parallel combination of $R_{p,d,O^{2-}}$ and R_{p,d,H^+}, presented as $R_{p,d}$ in Figure 10. This parallel combination will yield an apparent E_A in the temperature interval 600-750 °C between 85 and 150 kJ mol^{-1}.

4.3.2 Charge transfer resistance

The oxygen reduction reaction mechanism for LSM on YSZ was studied by Horita et al. by means of isotope imaging of O^{18} patterns on the YSZ surface after cathodic polarization of a dense LSM mesh [7]. The results showed that the reaction at 700 °C mainly takes place at the tpb, but that there is contribution also from bulk transport of O^{2-} through LSM in the volume close to the tpb. At high temperatures, this bulk transport will increase, and given the increased O^{2-} transport also in LWO, it can be expected an extended reaction zone around the tpb at high temperatures. This will give a higher apparent attempt rate value for $R_{p,ct,O^{2-}}$ at the highest temperatures. A gradual shift in attempt rate with increasing temperature is not accounted for in the model presented in this work. Therefore, the parameters reported for $R_{p,ct,O^{2-}}$ in this study should be regarded as first approximation average values only. The previously reported enthalpy of 181 kJ mol^{-1} for the charge transfer reaction on LSM / LWO in the high temperature region [11] has not been confirmed by this study. Regardless of fitting model, the high temperature $R_{p,ct}$ appears, according to our findings to exhibit an activation energy well below 100 kJ mol^{-1} in the temperature interval 650-900 °C. The activation energy for the charge transfer reaction in the intermediate temperature range is previously reported to 92 kJ mol^{-1} for LSM on LWO [10], in good agreement with our findings. All in all, the charge transfer resistance gives a minor contribution to R_p at temperatures below 800 °C. $R_{p\,ct}$ represents charge transfer occurring at the tpb, whether it is facilitated by oxide ions or protons.

4.4 Dependencies on pO_2

Impedance spectra taken at 700-900 °C on the symmetrical non-infiltrated electrode show multiple processes in the electrode frequency domain. The electrode response consists of several overlapping arcs that are seen more or less explicitly under the various conditions. Figure 14 shows fitting at 700 °C and pO_2 = 1 atm, and how the deconvolution model presented in Figure 5 can be supplied with one extra parallel R/CPE combination and fitted to the measured data of the symmetrical cell. Figure 15 gives the extended deconvolution model. The Gerischer circuit element readily accounts for concentration dependent impedance at the lowest frequencies, seen most explicitly at the lowest pO_2 and temperatures. In addition, there is a second arc emerging in the relaxation regime associated with a surface process at 700 °C. The two diffusion related resistances seen at 700 °C are labelled $R_{p,d,I}$ and $R_{p,d,II}$, and are associated with pseudo capacitance values in the range of 0.1-10 mFcm^{-2}, respectively. The DC Gerischer resistance, $Z_G'(\omega = 0)$, has up until now been added to $R_{p,d}$ when presenting the impedance data. In the following, it is more reasonable to present $R_{p,d,I}$ as one partial low frequency resistance, and add the Gerischer resistance to the second, $R_{p,d,II}$. Figure 16 gives the dependencies on pO_2 for the three partial polarization resistances, $R_{p,ct}$, $R_{p,d,I}$ and $R_{p,d,II}$ at 700 °C. The charge transfer resistance is pO_2-independent, while the exponent n in $R_{p,d,I} \propto pO_2^{-n}$ is approaching 1/2 at intermediate to high pO_2. For $R_{p,d,II}$, n is around 1/3. Values of n between 1/2 and 1/3 are indicative of surface reactions involving dissociative adsorption and surface diffusion. The area-specific pseudo-capacitance values are lower for $R_{p,d,I}$ than for $R_{p,d,II}$, indicating rather a surface diffusion process than dissociative adsorption as rate limiting for $R_{p,d,I}$. The charge transfer reaction at the electrolyte/electrode interface is in the literature generally reported as pO_2-independent both for PCFCs and SOFCs, in agreement with our findings. In Figure 17, the various contributions to the diffusion related resistance is summed up at 700, 800 and 900 °C and presented as $R_{p,d}$ vs pO_2 for each temperature. The diffusion resistance exhibits n-values between 1/3 and close to 1/2 in the pressure and temperature range investigated, suggesting that

different elementary reaction steps might influence the diffusion resistance over the temperature range. The middle frequency diffusion resistance, $R_{p,d,I}$, cannot be seen at 800 and 900 °C.

4.5 Conclusions

We have shown how the polarization resistance of a mixed proton / oxide ion conducting system can be characterised by the contributions of the two charge carriers. The measured polarization resistances were separated into partial resistances representing charge transfer and diffusion or surface related processes for protons and oxide ions and fitted to a model developed for a system of two ionic charge carriers with parallel pathways across electrolyte and electrodes. The composite electrode $La_{0.8}Sr_{0.2}MnO_3$ (LSM) / $La_{27.15}W_{4.85}O_{55.28}$ (La/W ≈ 5.60; LWO56) has been characterized from 900 °C, where LWO56 is mainly oxide ion conducting, to 450 °C where it is purely proton conducting. The composite electrode was infiltrated with Pt nanoparticles with average diameter of 5 nm, which lowered the total polarization resistance from 260 to 40 Ωcm^2 at 650 °C. The results showed that the LSM/LWO56 composite electrode is rate limited by diffusion below 900 °C, also when activated by nanoparticles of Pt. At high temperatures, the oxide ion related diffusion resistance, $R_{p,d,O^{2-}}$ with activation energy of ~150 kJ mol^{-1} dominates the polarization resistance, while a surface process directly or indirectly involving protons and with a lower activation energy of ~90 kJ mol^{-1}, R_{p,d,H^+}, dominates the polarization of the electrode at temperatures below 650 °C. The resistance associated with the oxide ion surface reaction exhibits a lower pre-exponential value (high attempt rate) and this is explained by an extended reaction zone for the oxide ions compared with protons. The results of the fitting showed that while the oxide ion reaction at high temperatures exhibits activation energies similar to reported literature values, the low temperature proton reaction exhibits lower activation energy than what is generally reported for LSM without differentiating between charge carriers. The electrochemical current, involving both oxide ions and protons, appears to pass through the triple phase boundary line, although the bulk path of oxide ions probably comes into play at the highest temperatures. Dependencies on pO_2 support the assignments of $R_{p,ct}$ and $R_{p,d}$ to charge transfer and diffusion or surface related processes, respectively.

Figures

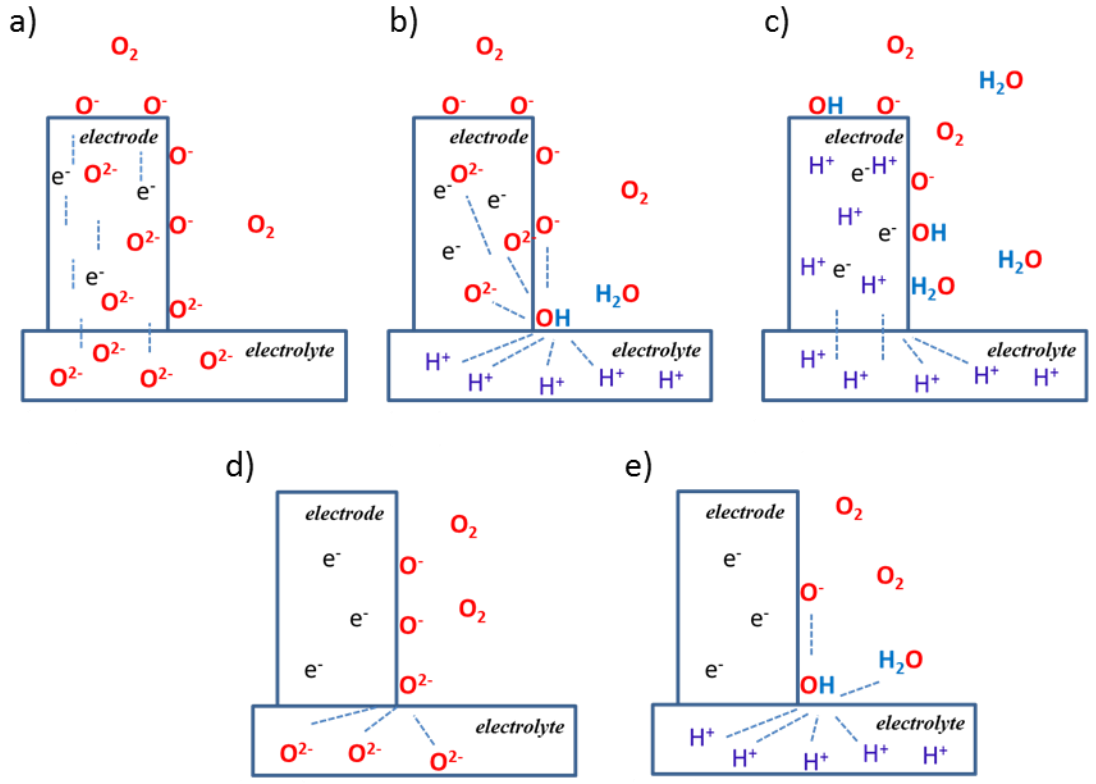

Figure 1: Illustration of reaction paths in an O-MIEC electrode on an oxide ion conductor electrolyte (a), an O-MIEC on a proton conductor (b), a P-MIEC on a proton conductor electrolyte (c), a pure electron conductor on an oxide-ion conductor (d), and a pure electron conductor on a proton conductor electrolyte (e).

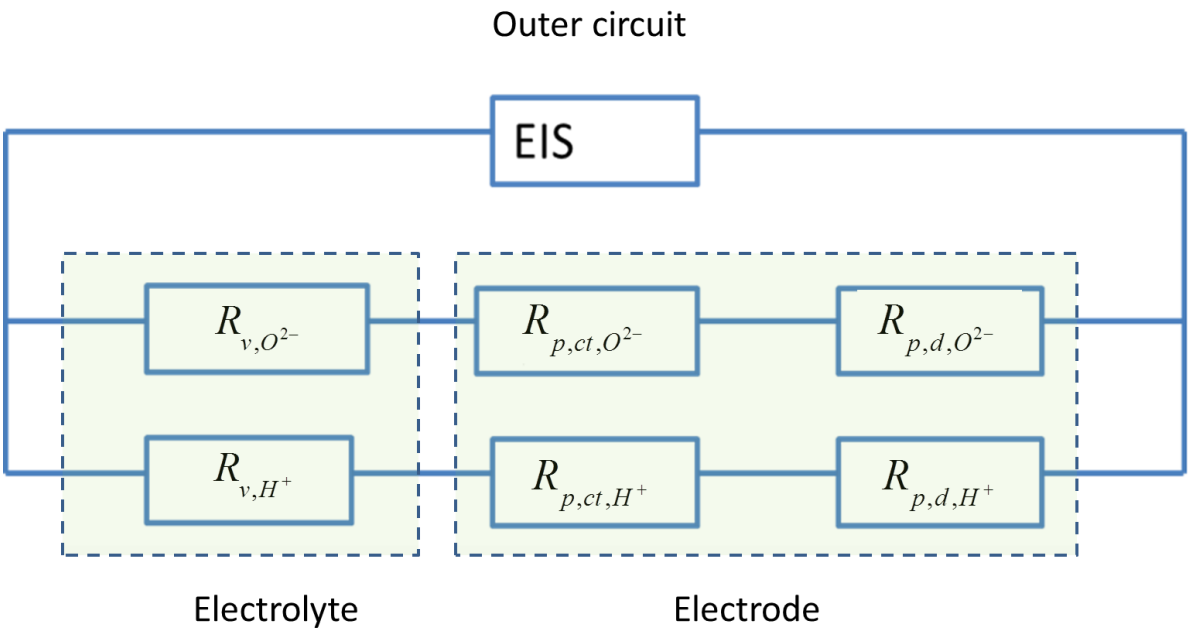

Figure 2: Electrical circuit sketch with partial resistances in two parallel rails for charge transport. Each rail encompasses electrolyte volume (v) and electrode charge transfer (ct) and surface related diffusion/adsorption (d) processes.

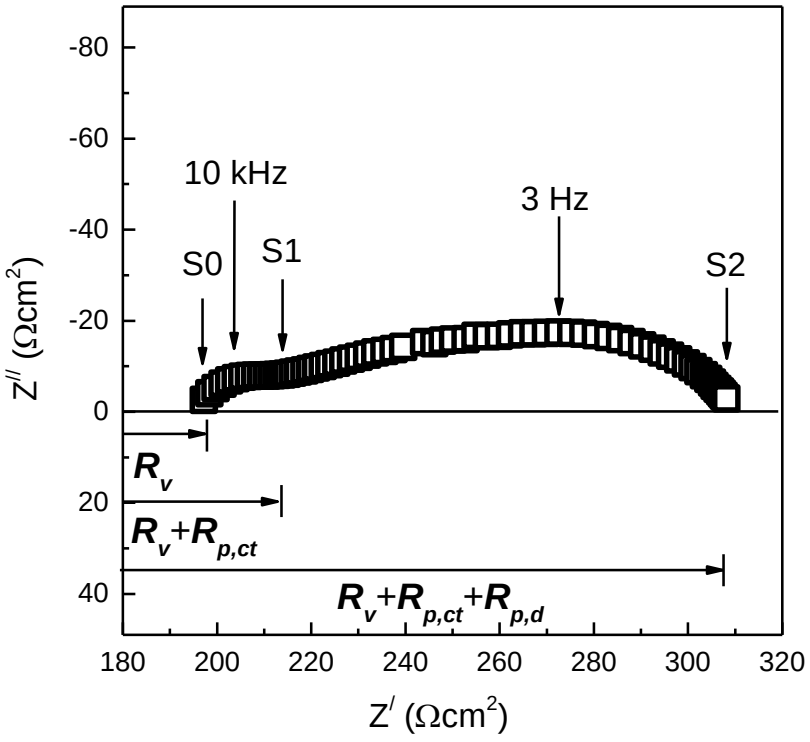

Figure 3: Impedance sweep of the Pt-infiltrated LSM / LWO56 composite electrode at 600 °C in wet oxygen.

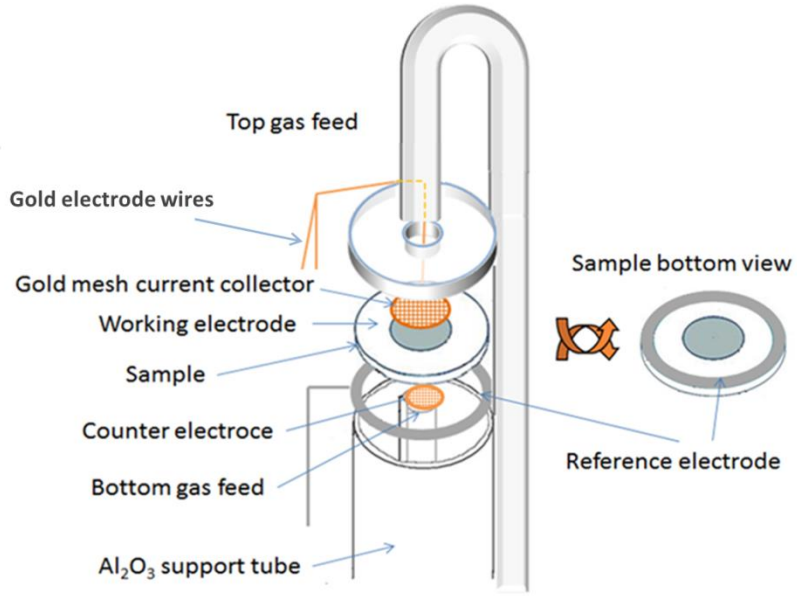

Figure 4: Set-up in the measurement cell.

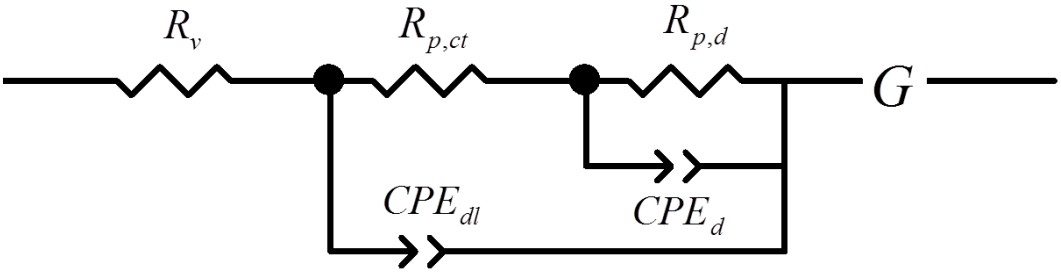

Figure 5: Deconvolution model with R_v representing electrolyte ionic resistance and, $R_{p,ct}/CPE_{dl}$ and $R_{p,d}/CPE_d$ representing two elementary electrode reaction steps and *G* representing the low frequency Gerischer impedance.

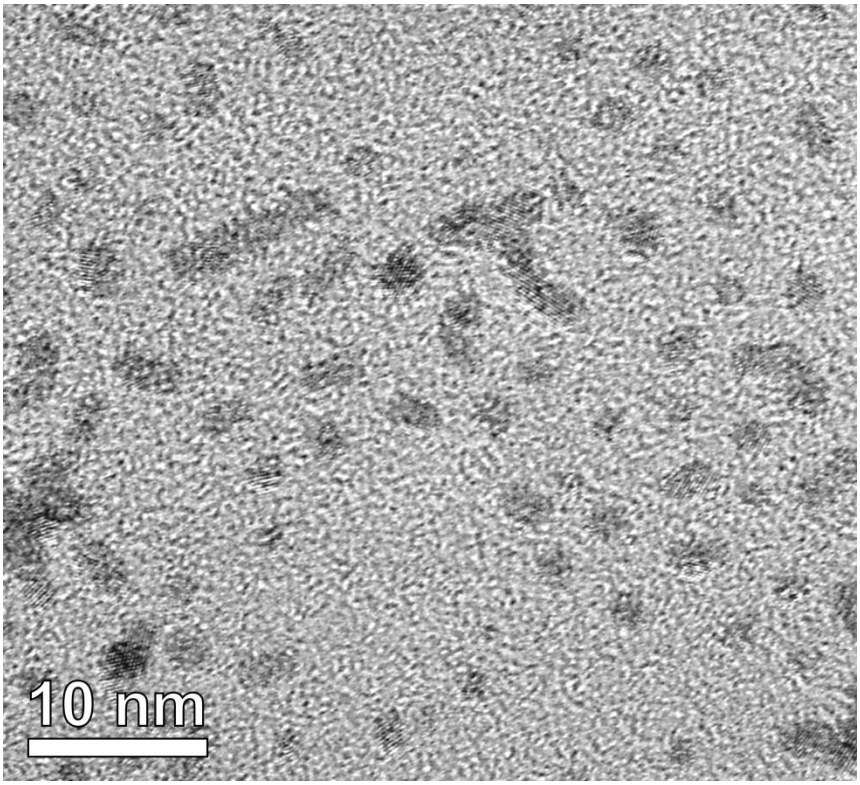

Figure 6: HRTEM micrograph of synthesized Pt nanoparticles situated on the amorphous carbon support film of the TEM grid.

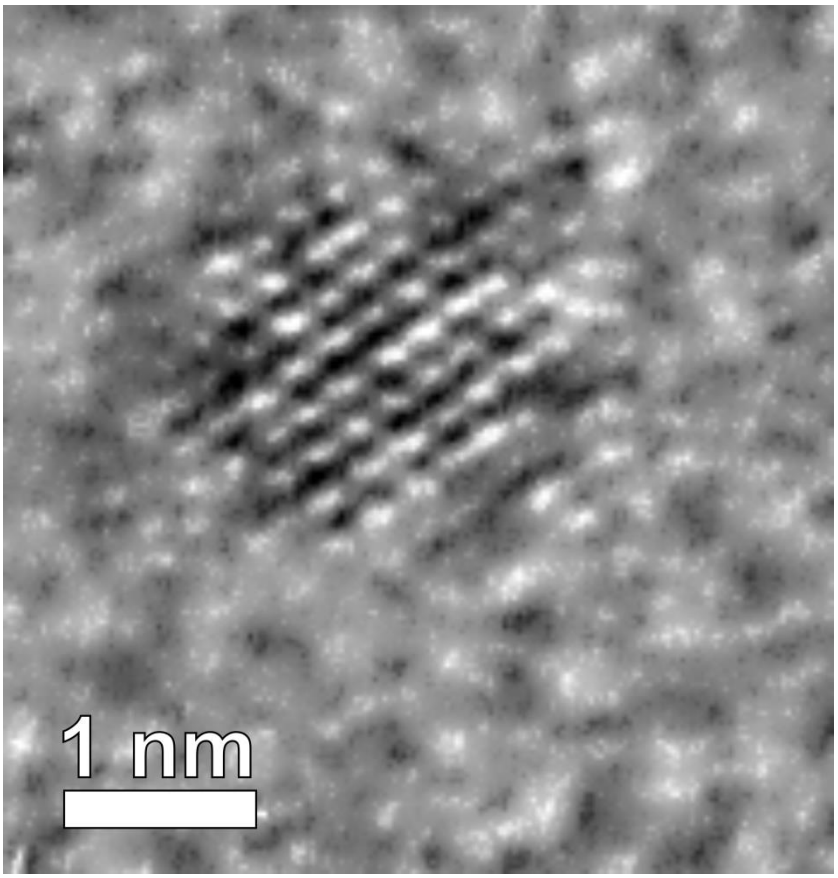

Figure 7: HRTEM micrograph of one Pt nanoparticle exhibiting lattice fringes. The particle is situated on the amorphous carbon film support film of the TEM grid.

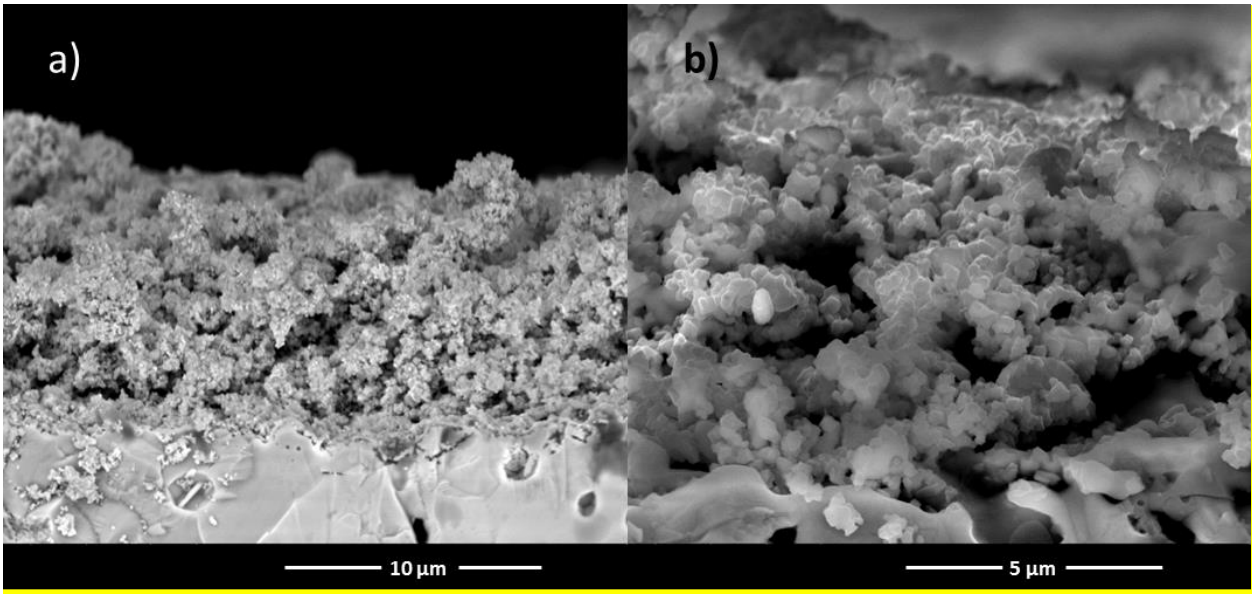

Figure 8: Cross-sectional micrographs of electrode layers on symmetric sample (a) and Pt-infiltrated sample (b).

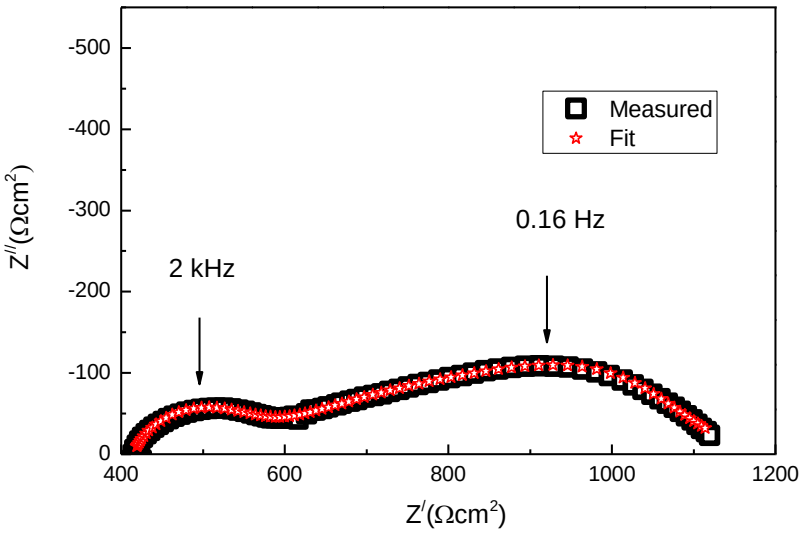

Figure 9: Impedance sweep (open squares) with fit (stars) for the Pt-infiltrated sample at 500 °C in wet oxygen.

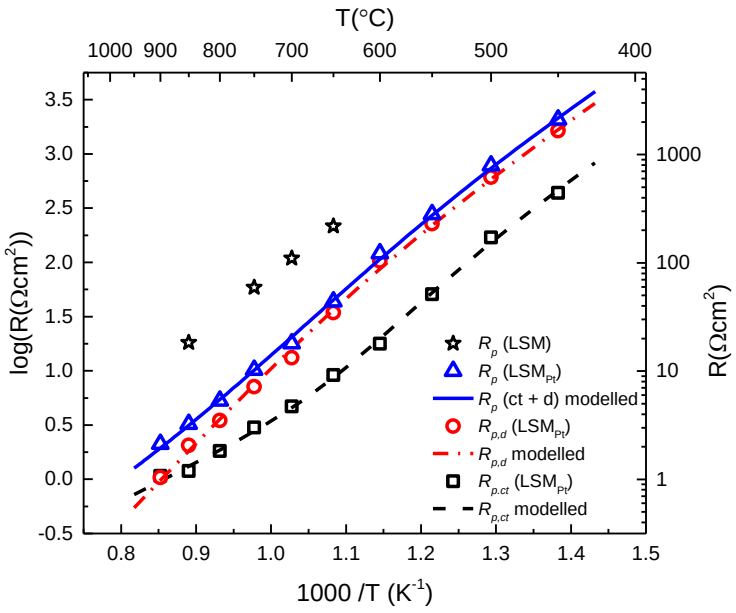

Figure 10: Polarization resistance, R_p, of the non-infiltrated (stars) and Pt infiltrated (triangles) LSM/LWO56 electrode, fitted to the modelled serial sum of $R_{p,ct}$ and $R_{p,d}$ (solid line). Deconvoluted partial polarization resistances, $R_{p,ct}$ (squares) and $R_{p,d}$ (circles) are fitted to equations 2 and 3, shown as dashed lines.

Table 1: Fitting parameters for partial resistances after fitting equation 2 and 3 to $R_{p,ct}$ and $R_{p,d}$.

Partial resistance	R^0(Ω cm^2)	E_A(kJ mol^{-1})
R_{p,ct,H^+}	$2.6 \cdot 10^{-4}$	85
R_{p,d,H^+}	$1.0 \cdot 10^{-3}$	90
$R_{p,ct,O^{2-}}$	$2.6 \cdot 10^{-4}$	85
$R_{p,d,O^{2-}}$	$3.5 \cdot 10^{-7}$	150

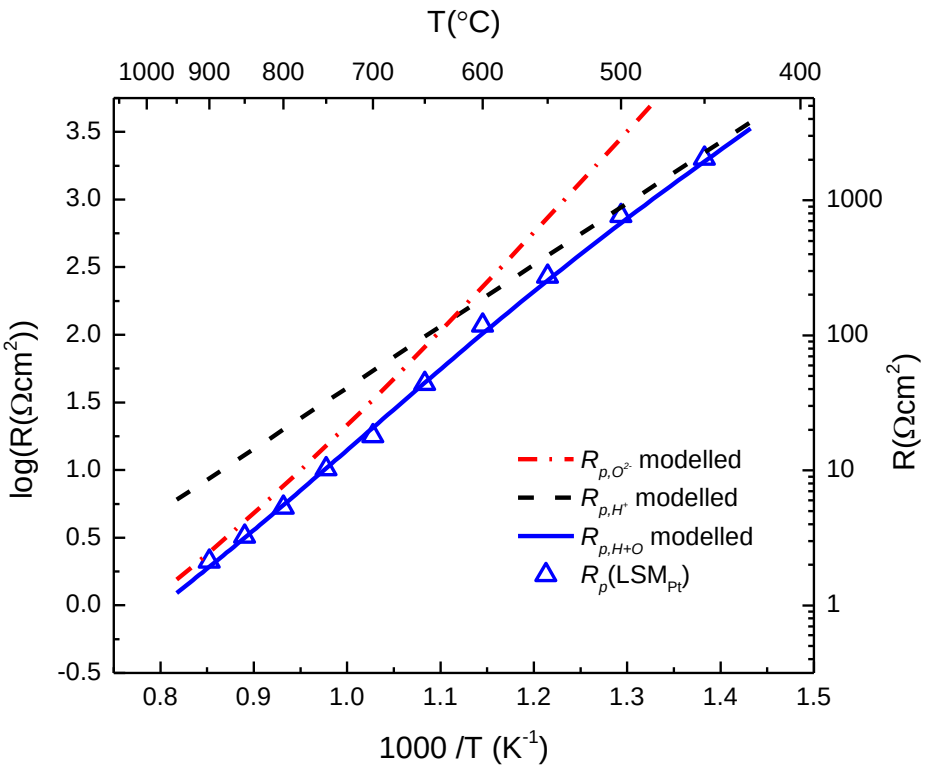

Figure 11: Pt infiltrated LSM/LWO56 electrode: Modelled electrode polarization for the individual transport rails of protons and oxide ions, R_{p,H^+} and $R_{p,O^{2-}}$ according to the parallel transport model presented in Equations 2 and 3 (dashed lines). Solid line and open triangles are modelled and measured total R_p, respectively.

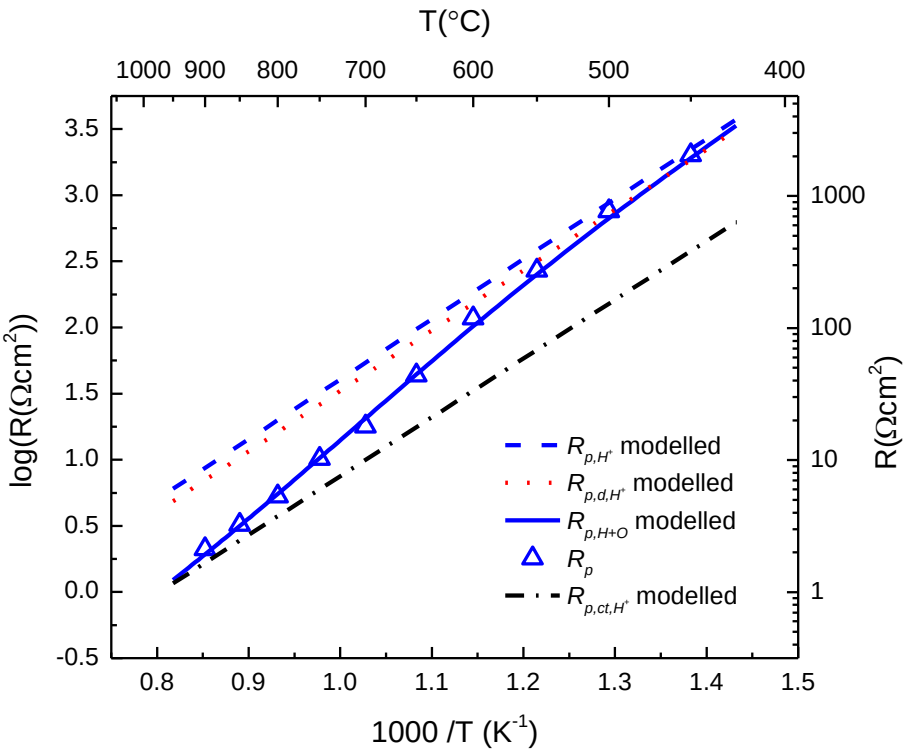

Figure 12: Pt infiltrated LSM/LWO56 electrode: Total and partial polarization resistances in the proton transport rail, R_{p,H^+}, R_{p,ct,H^+} and R_{p,d,H^+} according to the parallel transport model presented in Equations 2 and 3 (dashed lines). Solid line and open triangles are modelled and measured total R_p, respectively.

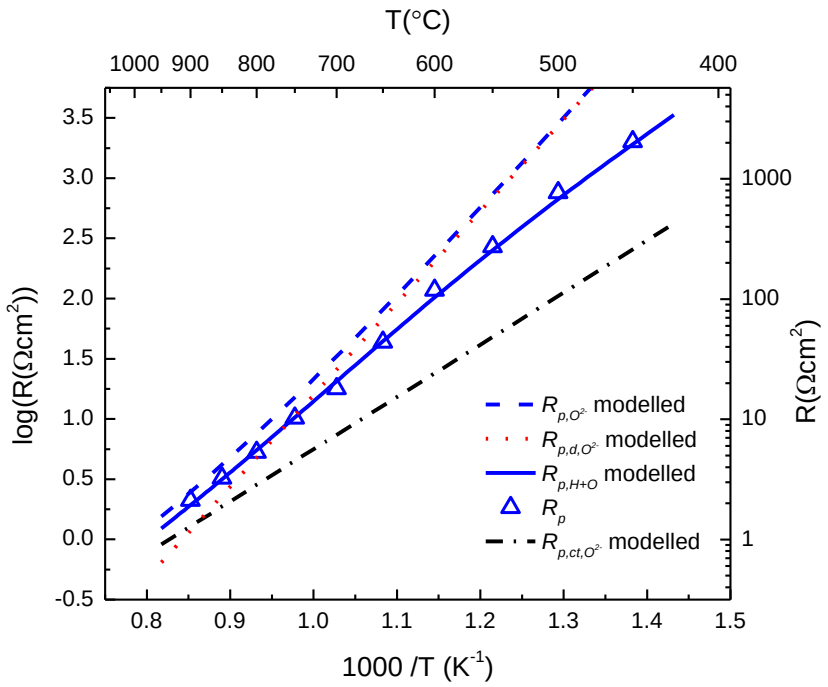

Figure 13: Pt infiltrated LSM/LWO56 electrode: Total and partial polarization resistances in the oxide ion transport rail, $R_{p,O^{2-}}$, $R_{p,ct,O^{2-}}$ and $R_{p,d,O^{2-}}$ according to the parallel transport model presented in Equations 2 and 3 (dashed lines). Solid line and open triangles are modelled and measured total R_p, respectively.

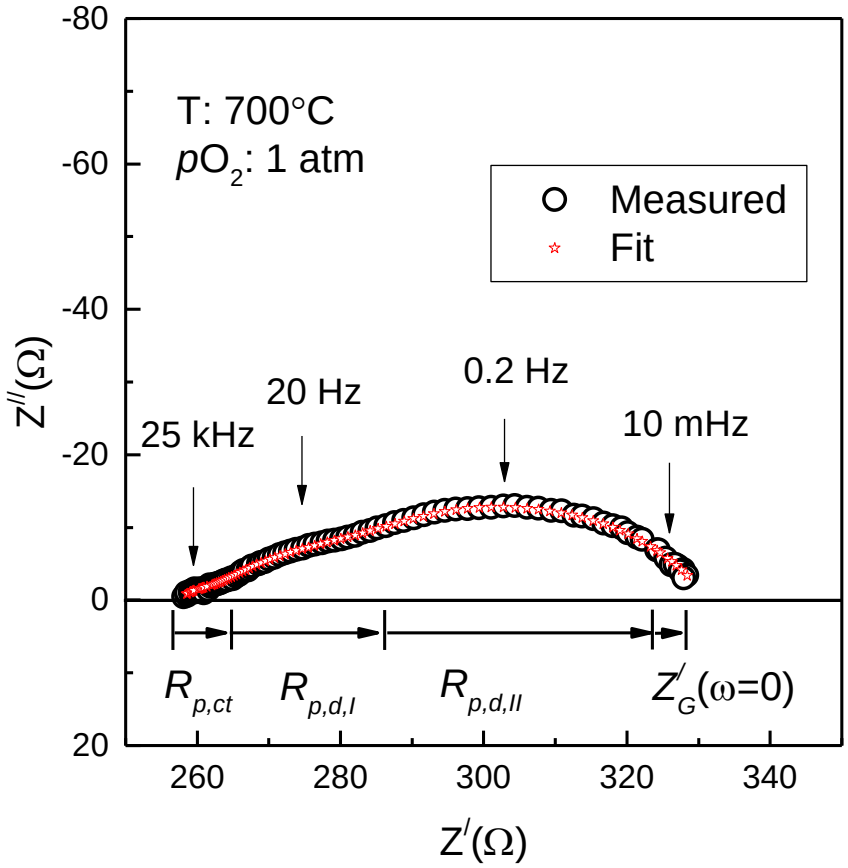

Figure 14: Deconvolution of impedance spectra taken on symmetrical cell of LSM / LWO56 // LWO56 // LSM / LWO56 at 700 °C, pH_2O = 0.027 atm and pO_2 = 1 atm. Open circles are measured values, red stars represent fit to deconvolution.

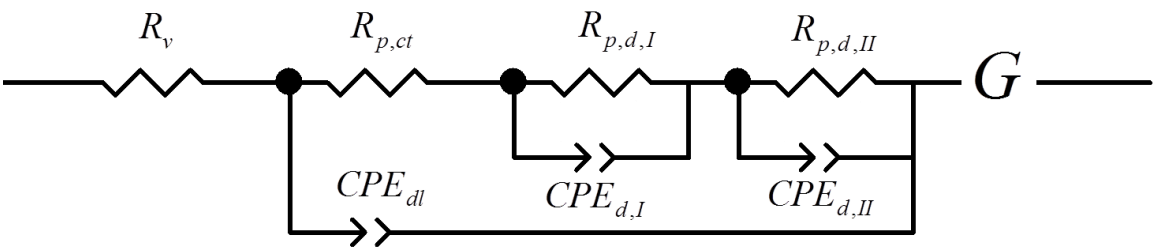

Figure 15: Extended deconvolution model for three partial polarization resistances.

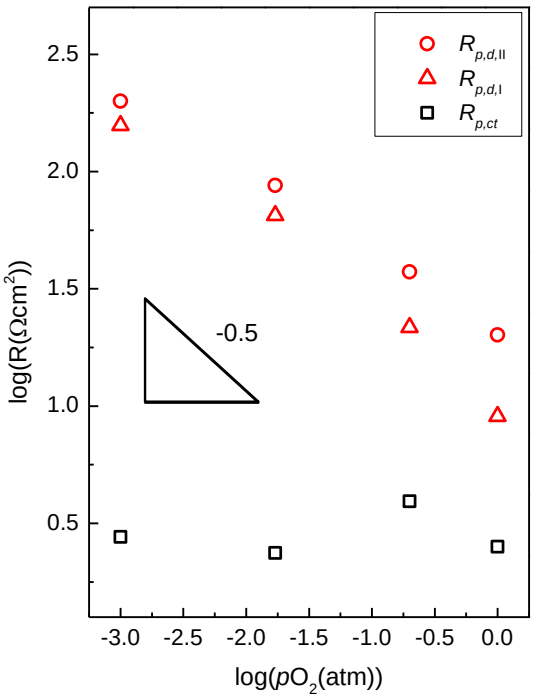

Figure 16: Partial polarization resistances for non-infiltrated electrode vs pO_2 at 700 °C.

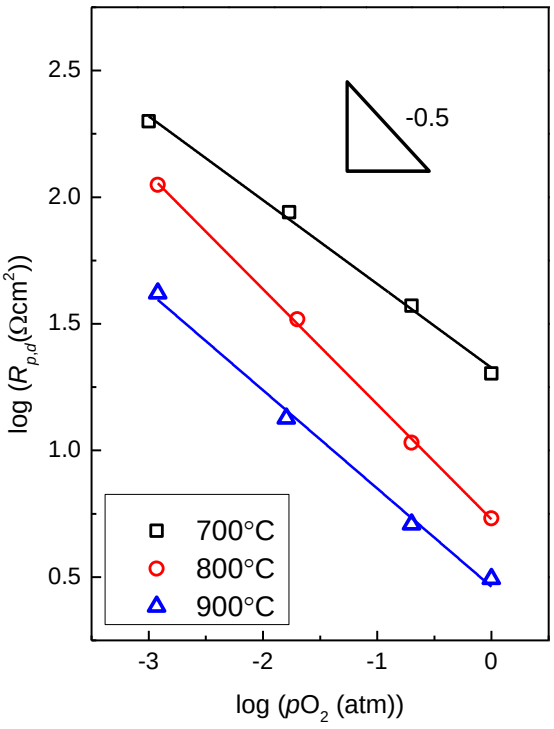

Figure 17: Total diffusion-related polarization resistance, $R_{p,d}$ vs pO$_2$ at 700, 800 and 900 °C.

References

[1] E. Fabbri, D. Pergolesi, E. Traversa, *Science and Technology of Advanced Materials* **11** (2010) (4) 044301.

[2] C. Duan, J. Tong, M. Shang, S. Nikodemski, M. Sanders, S. Ricote, A. Almansoori, R. O'Hayre, *Science* **349** (2015) (6254) 1321.

[3] D. Poetzsch, R. Merkle, J. Maier, *Faraday Discussions* **182** (2015) (0) 129.

[4] R. Strandbakke, V.A. Cherepanov, A.Y. Zuev, D.S. Tsvetkov, C. Argirusis, G. Sourkouni, S. Prünte, T. Norby, *Solid State Ionics* **278** (2015) 120.

[5] J. Mizusaki, Y. Yonemura, H. Kamata, K. Ohyama, N. Mori, H. Takai, H. Tagawa, M. Dokiya, K. Naraya, T. Sasamoto, H. Inaba, T. Hashimoto, *Solid State Ionics* **132** (2000) (3–4) 167.

[6] J. Fleig, H.R. Kim, J. Jamnik, J. Maier, *Fuel Cells* **8** (2008) (5) 330.

[7] T. Horita, K. Yamaji, M. Ishikawa, N. Sakai, H. Yokokawa, T. Kawada, T. Kato, *Journal of The Electrochemical Society* **145** (1998) (9) 3196.

[8] P. Plonczak, D.R. Sørensen, M. Søgaard, V. Esposito, P.V. Hendriksen, *Solid State Ionics* **217** (2012) 54.

[9] F.H. van Heuveln, H.J.M. Bouwmeester, *Journal of The Electrochemical Society* **144** (1997) (1) 134.

[10] E. Quarez, K.V. Kravchyk, O. Joubert, *Solid State Ionics* **216** (2012) 19.

[11] C. Solis, L. Navarrete, S. Roitsch, J.M. Serra, *Journal of Materials Chemistry* **22** (2012) (31) 16051.

[12] J. Nielsen, J. Hjelm, *Electrochimica Acta* **115** (2014) 31.

[13] J. Jamnik, J. Maier, *Physical Chemistry Chemical Physics* **3** (2001) (9) 1668.

[14] H. Fjeld, R. Haugsrud, A.E. Gunnæs, T. Norby, *Solid State Ionics* **179** (2008) (33–34) 1849.

[15] A. Magraso, J.M. Polfus, C. Frontera, J. Canales-Vazquez, L.-E. Kalland, C.H. Hervoches, S. Erdal, R. Hancke, M.S. Islam, T. Norby, R. Haugsrud, *Journal of Materials Chemistry* **22** (2012) (5) 1762.

[16] S. Erdal, L.-E. Kalland, R. Hancke, J. Polfus, R. Haugsrud, T. Norby, A. Magrasó, *International Journal of Hydrogen Energy* **37** (2012) (9) 8051.

[17] T. Norby, R. Haugsrud, *Membranes for Energy Conversion*, Wiley-VCH Verlag GmbH & Co. KGaA (2008), p.169-216.

[18] R. Hancke, A. Magrasó, T. Norby, R. Haugsrud, *Solid State Ionics* **231** (2013) (0) 25.

[19] C.-S. Lin, M.R. Khan, S.D. Lin, *Journal of Colloid and Interface Science* **299** (2006) (2) 678.

[20] A. Kumar, H. Joshi, A. Mandale, R. Srivastava, S. Adyanthaya, R. Pasricha, M. Sastry, *J Chem Sci* **116** (2004) (5) 293.

[21] P. Plonczak, D.R. Sørensen, M. Søgaard, V. Esposito, P.V. Hendriksen, *Solid State Ionics* **217** (2012) (0) 54.

[22] R.A. De Souza, J.A. Kilner, *Solid State Ionics* **106** (1998) (3–4) 175.

[23] E.P. Murray, T. Tsai, S.A. Barnett, *Solid State Ionics* **110** (1998) (3–4) 235.

[24] Y.J. Leng, S.H. Chan, K.A. Khor, S.P. Jiang, *Journal of Solid State Electrochemistry* **10** (2006) (6) 339.

[25] X.G. Cao, S.P. Jiang, *International Journal of Hydrogen Energy* **38** (2013) (5) 2421.

[26] R. Strandbakke, M. F. Sunding, T. Norby., *To be published.*